Nanoparticles |*Hot Paper*|

Smart *Shell-by-Shell* Nanoparticles with Tunable Perylene Fluorescence in the Organic Interlayer

Lisa M. S. Stiegler,[a] Stefanie Klein,[b] Carola Kryschi,[b] Winfried Neuhuber,[c] and Andreas Hirsch*[a]

Abstract: A new series of *shell-by-shell* (*SbS*)-functionalized Al_2O_3 nanoparticles (NPs) containing a perylene core in the organic interlayer as a fluorescence marker is introduced. Initially, the NPs were functionalized with both, a fluorescent perylene phosphonic acid derivative, together with the lipophilic hexadecylphosphonic acid or the fluorophilic (1 H,1 H,2 H,2H-perfluorodecyl)phosphonic acid. The lipophilic first-shell functionalized NPs were further implemented with amphiphiles built of aliphatic chains and polar head-groups. However, the fluorophilic NPs were combined with amphiphiles consisting of fluorocarbon tails and polar head-groups. Depending on the nature of the combined phosphonic acids and the amphiphiles, tuning of the perylene fluorescence can be accomplished due variations of supramolecular organization with the shell interface. Because the *SbS*-functionalized NPs dispose excellent dispersibility in water and in biological media, two sorts of NPs with different surface properties were tested with respect to biological fluorescent imaging applications. Depending on the agglomeration of the NPs, the cellular uptake differs. The uptake of larger agglomerates is facilitated by endocytosis, whereas individualized NPs cross directly the cellular membrane. Also, the larger agglomerates were preferentially incorporated by all tested cells.

Introduction

Over the last years, our group established for the first time a highly hierarchical structured functionalization concept for metal oxide NPs (Scheme 1), which is based on a combination of two functionalization steps.[1] In the first step, a wet-chemical functionalization process takes place, where a metal oxide NP surface is treated with phosphonic acid derivatives, resulting in covalent binding between the organic molecules and the inorganic core.[2] In the next step, an attachment of amphiphiles around first-shell functionalized NPs follows, which is based on the self-assembly provided by solvophobic interactions of the apolar moiety of the amphiphiles interdigitating into the first ligand shell of the NPs. The polar moieties pointed outwards and create water-dispersible character of the corresponding hybrids.[3]

This field of NP functionalization was extended recently, with new implications and applications. First, this functionalization principle of metal oxide NPs was used to generate a switchable dispersibility behavior of NPs in fluorocarbons, hydrocarbons, and water and further allows the tuning of surface energies of NP surfaces, for example, from hydrophilic to superhydrophobic, from lipophilic to lipophobic, from fluorophil-

[a] *L. M. S. Stiegler, Prof. Dr. A. Hirsch*
Department of Chemistry & Pharmacy
Chair of Organic Chemistry II
Friedrich-Alexander University of Erlangen-Nuremberg
Nikolaus-Fiebiger-Straße 10, 91058 Erlangen (Germany)
E-mail: andreas.hirsch@fau.de

[b] *Dr. S. Klein, Prof. Dr. C. Kryschi*
Department Chemistry and Pharmacy
Physical Chemistry I and ICMM
Friedrich-Alexander University of Erlangen-Nuremberg
Egerlandstraße 3, 91058 Erlangen (Germany)

[c] *Prof. Dr. W. Neuhuber*
Department of Anatomy
Chair of Anatomy I
Friedrich-Alexander University of Erlangen-Nuremberg
Krankenhausstraße 9, 91054 Erlangen (Germany)

Supporting information and the ORCID identification number(s) for the author(s) of this article can be found under: https://doi.org/10.1002/chem.202003232.

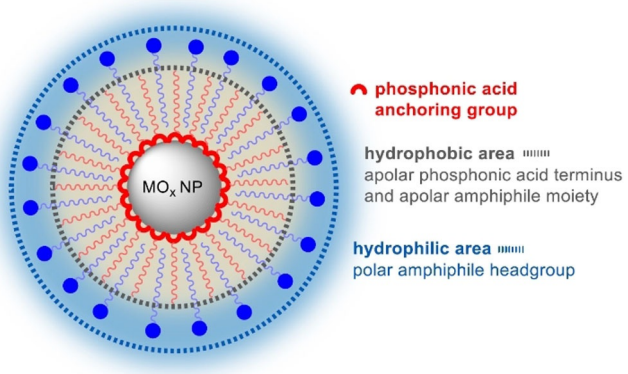

Scheme 1. General structure of *SbS*-functionalized NPs.

ic to fluorophobic.[4] We have also established a method, in which the fluorescence of a pyrene core coupled to a phosphonic acid attached covalently to a Al_2O_3 NP surface, could be quenched and turned on and off.[5] Therefore, the spacing phosphonic acids and amphiphiles were carefully selected in order to control the intermolecular interaction of the NP surface. By introducing an amphiphile with a pyridinium head-group, the fluorescence of the pyrene moiety was turned off and by removing the amphiphile from the *SbS*-structure, the fluorescence was switched on, again. Compounds involving pyridinium units cause a decrease in the fluorescence of alternant polycyclic aromatic hydrocarbons (PAHs), like pyrene or perylene, in polar solvents such as water and acetonitrile.[6] Responsible for the quenching is a photo-induced electron-transfer (PET) from the LUMO of the PAHs excited state towards the LUMO of the positively charged nitrogen atom of the pyridinium unit, that has a lower energy level.[7] Recently, we demonstrated that the type and nature of spacing phosphonic acids influences the aggregation of perylene bisimides (PBIs) onto Al_2O_3 NP surfaces and thus the optical properties of the PBIs.[8] Whereas the rigid fluorocarbon phosphonic acids separate the PBI units very effectively, interactions of PBIs with hydrocarbon phosphonic acids are less hindered. The highly flexible glycol phosphonic acids lead to the weakest hindered interaction causing strong aggregation. We also reported on *SbS*-functionalized NPs with electronic communication between the first and second-layer interface.[9] In a *lego-type* principle, electron-donors were combined with electron-acceptors, which resulted on one hand in electronical communications between the chromophores with different electron demand and on the other hand, the optical properties of the NPs changed. Because of the excellent water dispersibility and stability of *SbS*-functionalized NPs with interdigitating amphiphiles containing polar head-groups, also some biological applications were already reported.[10] Initially coated hydrophobic Au-Fe_3O_4 nano-heterodimers (NHDs) that were capped with oleic acid, were encapsulated in a self-assembled bilayer shell formation with 1-octadecylpyridinium, or 4-dodecylbenzenesulfonate, to provide a positive or negative surface charge onto the NP surface. We recognized, that the surface charge as well as the surface architecture of the NHDs influenced the mechanism and the efficiency of the cellular uptake pathway, cellular localization, and the toxicity of human tumor (MCF-7) and healthy epithelial (MCF-10 A) cells.[10]

Herein, we report on a series of *SbS*-functionalized Al_2O_3 NPs, involving a perylene core as a fluorescence marker in the first ligand shell in combination with spacing phosphonic acids and amphiphiles of different nature resulting in diverse mutations of the initial perylene fluorescence. We created a hydrocarbon as well as a fluorocarbon analogue of Al_2O_3 NPs, by combining 10% **PAR^1** with 90% **PAR^2**, resulting in **Al_2O_3-(PAR$^1_{10\%}$ PAR$^2_{90\%}$)** NPs, or in the case of combining 10% **PAR^1** with 90% **PAR^3**, **Al_2O_3-(PAR$^1_{10\%}$ PAR$^3_{90\%}$)** NPs were formed. The hydrocarbon analogy was further implemented with amphiphiles built of aliphatic chains and polar head-groups (**SDBS**, **SDS**, **DDPB**, **DTAB**, **HC-PEG**), generating lipophilic environment around the perylene units. The fluorocarbon analogy was further implemented with amphiphiles consisting of fluorocarbon tails and polar head-groups (**PFUnDA**, **FC-PB**, **FC-PEG**), generating fluorophilic pockets. This allowed for tailoring the perylene fluorescence, from drastic increase of fluorescence by disaggregation of perylene excimers[11] onto the NP surface up to fluorescence quenching by forcing the perylene units in its excimeric form [12]. Drastic decrease of fluorescence was observed by combining the perylene functionalized NPs with amphiphiles containing a pyridinium head-group. The hydrocarbon analogy of the particles that were functionalized with **SDBS** or **DTAB** (contrary surface charge), namely **[(Al_2O_3-(PAR$^1_{10\%}$ PAR$^2_{90\%}$)]SDBS** and **[(Al_2O_3-(PAR$^1_{10\%}$ PAR$^2_{90\%}$)]DTAB**, were further used in fluorescence microscopy of the non-cancerous human umbilical vein endothelial cells (HUVEC) and breast epithelial cells (MCF-10 A) as well of the cancerous A549 (lung cancer) and MDA-MB-231 (breast cancer) cells. Further their biocompatibility, cellular uptake pathway and the intracellular NP content was studied.

Results and Discussion

Synthesis of the parent compounds

The stepwise synthesis of the so far unknown phosphonic acid **PAR^1** is outlined in Scheme 4. Whereas compounds **1** and **2** were known,[5] synthetic access to **3** and **PAR^1** had be established. The precursor molecule **1** was synthesized by a Michaelis–Arbuzov reaction of 1,12-dibromododecane with triethylphosphite and isolated as a pure compound in 26% yield. Compound **2** was generated by a nucleophilic substitution of the bromide in **1** with sodium azide in 96% yield. The azide functionality of the phosphonate-ester was subsequently subjected to a "click" reaction with 3-ethynyl perylene leading to the formation of **3** in 34% yield.[5,9,13] Final deprotection of **3** afforded the target molecule **PAR^1** in 80% yield.

Whereas the amphiphiles **SDBS**, **SDS**, **DTAB**, and **PFUnDA** are commercially available, we synthesized **DDPB**, **HC-PEG**, **FC-PB**, and **FC-PEG** according to literature procedures.[4a,5,14] The syntheses of the amphiphiles are outlined in Scheme 5. **DDPB** was synthesized by implementation of n-dodecyl bromide with pyridine and was received as a pure compound in 57% yield.[14a] **FC-PB** was generated via a two-step synthesis. In the first step, a Steglich esterification of 11-bromoundecanoic acid with heptadecafluorodecan-1-ol was performed, resulting in molecule **4** in 43% yield. Subsequently, **4** was refluxed in pyridine, resulting in 40% yield of **FC-PB**.[5] **HC-PEG** was afforded by implementation of lauric acid chloride with triethylene glycol, the reaction was catalyzed by triethylamine. The product was obtained in 61% yield. Towards **FC-PEG**, firstly, perfluoro-n-undecanoic acid was converted to the corresponding perfluoro-n-undecanoic acid chloride **5** by the help of thionyl chloride. Subsequently, **5** reacted with triethylene glycol, catalyzed by triethylamine, resulting in pure **FC-PEG** in 13% yield.[4a]

Assembly of the hydrocarbon SbS-functionalized NPs

The optical properties of the hydrocarbon *SbS*-functionalized **Al_2O_3-($PAR^1_{10\%}$ $PAR^2_{90\%}$)** NPs during the formation of a lipophilic pocket among the perylene units caused by the assembly of amphiphiles, were studied (Scheme 2, Scheme 3). The Al_2O_3 NPs are commercially available. As obtained from BET measurements they have an average diameter size of 14 nm. DLS measurements of the pristine NPs in IPA show a hydrodynamic diameter of <50 nm whereas the *SbS*-functionalized NPs in deionized water reach a hydrodynamic diameter of around 100 nm. Additional information on the Al_2O_3 NP core is given in the supporting information. For the functionalization procedure, 7.5 mL 0.15 wt% Al_2O_3 NP dispersions in isopropanol were mixed with 5 mL of a phosphonic acid solution in MeOH/toluene (1:1), resulting in a total concentration of the phosphonic acid mixture of 5 mM. Subsequently, 30 min. of ultrasonication and repeated washing with isopropanol/toluene/isopropanol followed, to achieve homogeneous surface functionalization and to remove excess of phosphonic acid. The value of 5 mM has already been proven for providing a full surface coverage of such metal oxide NPs with phosphonic acids.[9,15] With the results of TGA measurements, grafting densities of 4.29 nm^{-2} for the **Al_2O_3-($PAR^1_{10\%}$ $PAR^2_{90\%}$)** hybrids and 3.02 nm^{-2} for the **Al_2O_3-($PAR^1_{10\%}$ $PAR^2_{90\%}$)** hybrids were obtained (see Figure S3). The fact, that phosphonic acid mixtures can be stoichiometrically displayed onto metal oxide surfaces, was already corroborated in recent studies.[4b,5,8,9,15,16] TGA measurements of Al_2O_3 NPs functionalized with different ratios of PAR^1 and PAR^2/PAR^3 were shown in the supporting informa-

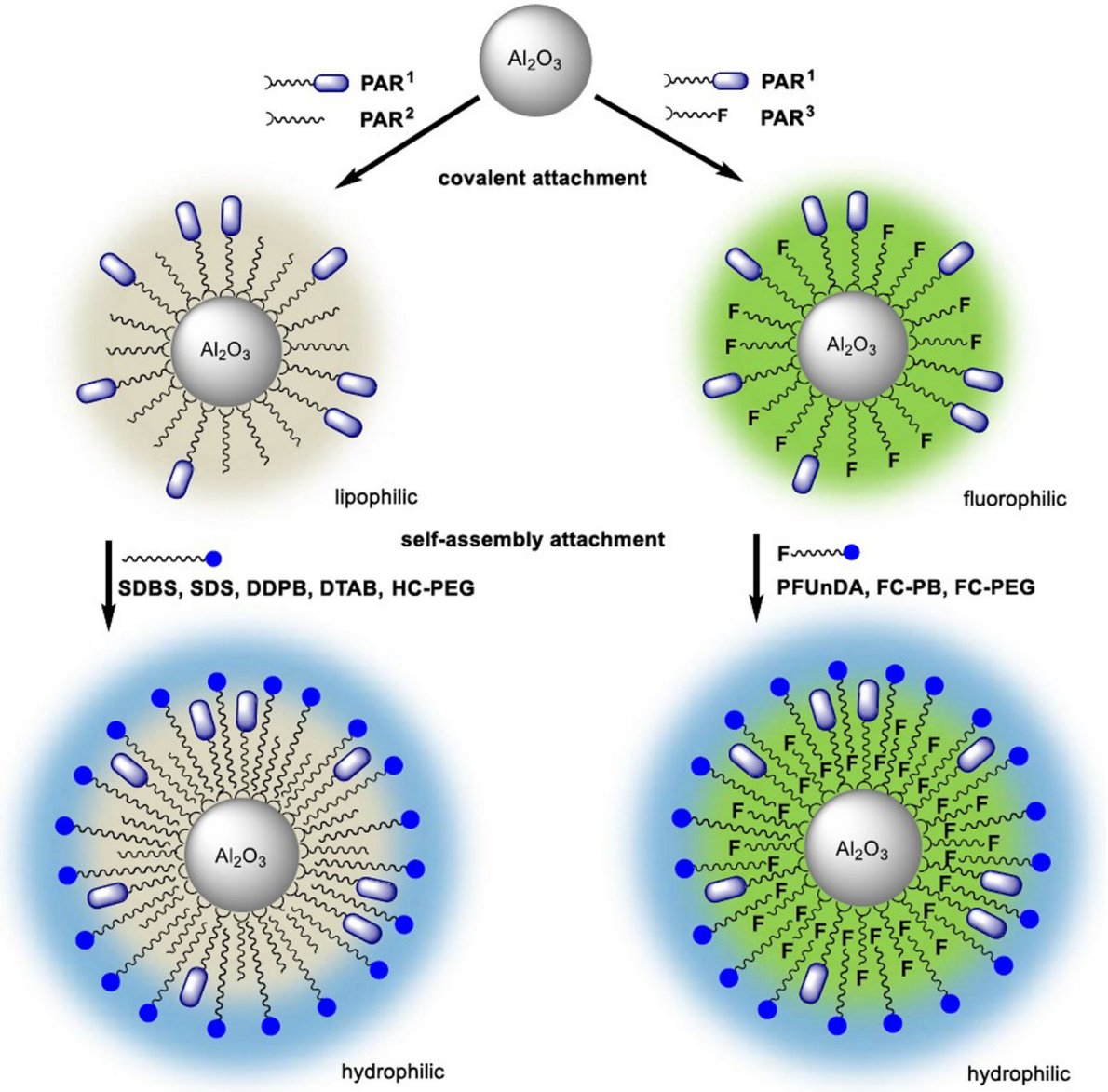

Scheme 2. Hydrocarbon and fluorocarbon based *SbS*-architectures consisting of aluminum oxide NP cores, the fluorescence marker **PAR^1**, the spacing phosphonic acids **PAR^2** and **PAR^3**, as well as the hydrocarbon-polar fused amphiphiles **SDBS**, **SDS**, **DTAB**, **HC-PEG** and the fluorocarbon-polar fused amphiphiles **PFUnDA**, **FC-PB**, **FC-PEG** (see also Scheme 3).

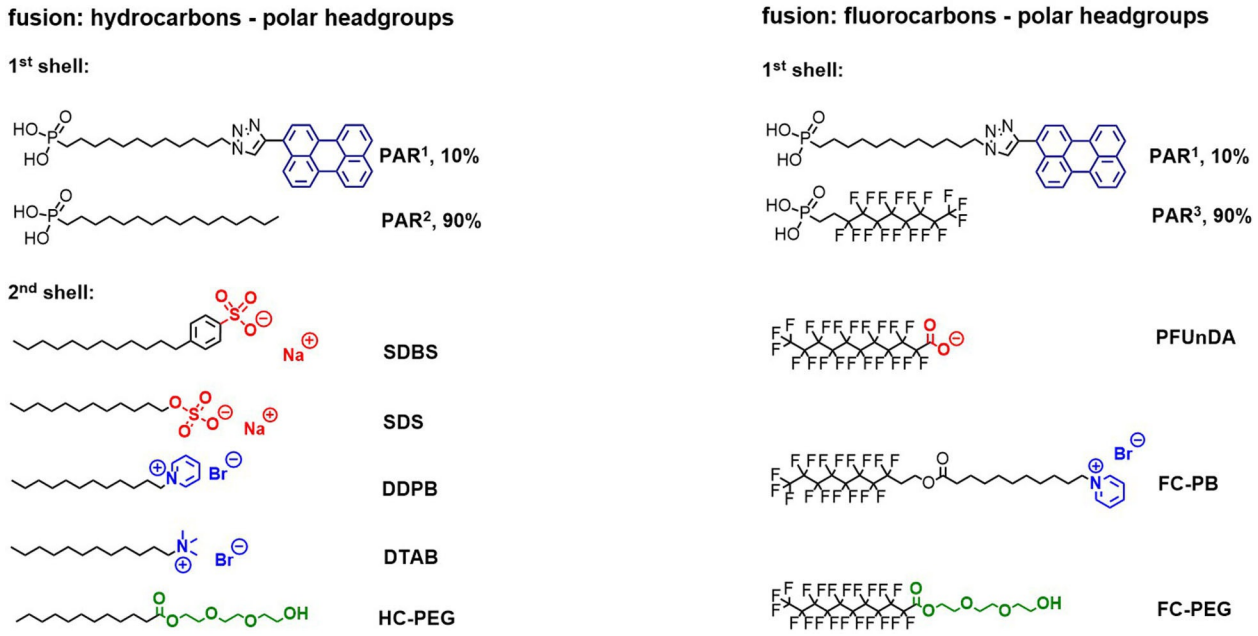

Scheme 3. Building blocks for the *SbS*-functionalization of aluminum oxide NPs with I) a mixture of **PAR^1** and **PAR^2** with the amphiphiles **SDBS**, **SDS**, **DDPB**, **DTAB**, **HC-PEG** (left column) and II) **PAR^1** and **PAR^3** with **PFUnDA**, **FC-PB**, **FC-PEG** (right column).

tion (Figure S3) and displayed the differences in the grafting densities as well as in the DTG curves. The coverage with **PAR^1** (Scheme 4) and **PAR^2** provides a lipophilic surface.[4a,17] The second ligand shell was assembled through the non-covalent interdigitation of the amphiphiles fused of a hydrocarbon moiety and a polar head-group, namely sodium dodecylbenzenesulfonate (**SDBS**), sodium dodecylsulfate (**SDS**), 1-dodecylpyridinium bromide (**DDPB**), (1-dodecyl)trimethylammonium bromide (**DTAB**), or 2-(2-(2-hydroxyethoxy)ethoxy)ethyl dodecanoate (**HC-PEG**, Scheme 5). The amphiphiles comprising the second ligand shell caused a polarity umpolung from lipophilic (**PAR^2**) to hydrophilic causing water-dispersibility.[4a] The formation of the second shell was monitored via fluorescence measurements. Therefore, 2 mL of 0.015 wt% **Al_2O_3-($PAR^1_{10\%}$ $PAR^2_{90\%}$)** were filled in a cuvette and were titrated with 0.015 wt% **[Al_2O_3-($PAR^1_{10\%}$ $PAR^2_{90\%}$)]20 mM** amphiphile dispersions, resulting in a concentration range from zero up to 10 mM amphiphile with a constant 0.015 wt% concentration of first-shell functionalized NPs. The constant concentration of first-shell functionalized NPs is crucial for excluding dilution effects during titration, so that the changes in the fluorescence spectra can be assigned exclusively to the addition of amphiphile. Exactly the same titration procedure was applied for all other examples (Scheme 2, Scheme 3).

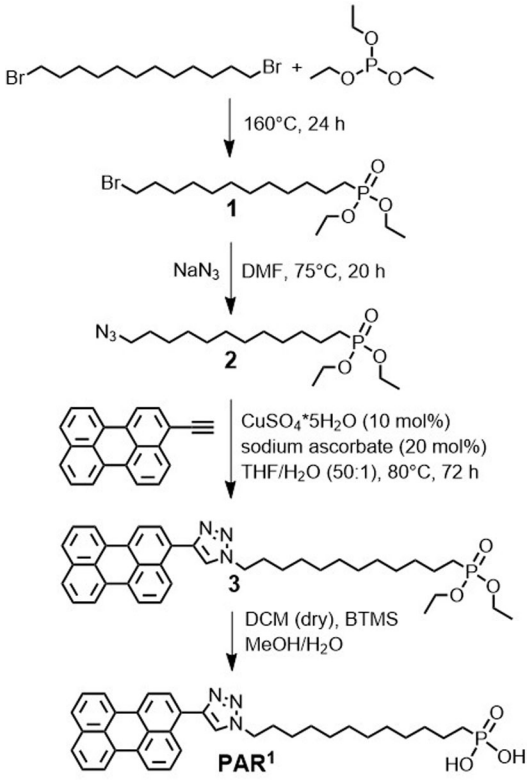

Scheme 4. Synthesis of the phosphonic acid **PAR^1**.

Figure 1 a, b, c shows the fluorescence and UV/Vis spectra of **Al_2O_3-($PAR^1_{10\%}$ $PAR^2_{90\%}$)** NP dispersions, that were titrated with **[Al_2O_3-($PAR^1_{10\%}$ $PAR^2_{90\%}$)]20 mM SDBS** dispersions (Scheme 6). The NPs **Al_2O_3-($PAR^1_{10\%}$ $PAR^2_{90\%}$)** without **SDBS** give raise to weak fluorescence signals with weak and undefined 0–0* and 0–1* transition bands and a missing 0–2* transition band. During titration with **SDBS**, the overall fluorescence intensity of the perylene unit increased. The intensity of the 0–0* transition at 469 nm increased strongest, then the intensity of the 0–1* transition at 499 nm, and also the signal of the 0–2* transition at 537 nm appeared. By titrating **SDBS** to the **Al_2O_3-($PAR^1_{10\%}$ $PAR^2_{90\%}$)** NPs, of course, the intensities of the absorption bands of the benzene moieties of **SDBS** at 255 and 261 nm increased, whereas the characteristic absorption sig-

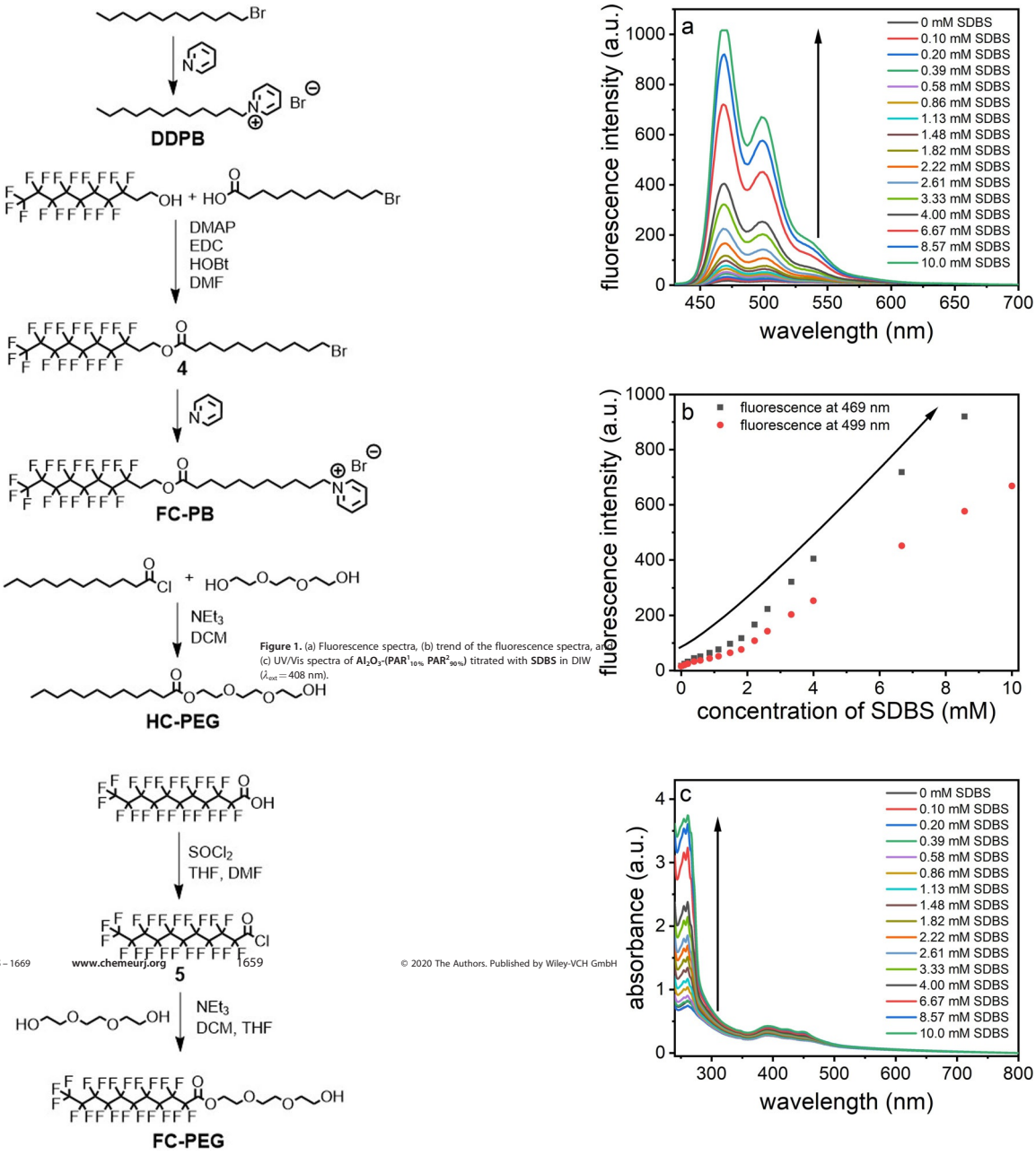

Figure 1. (a) Fluorescence spectra, (b) trend of the fluorescence spectra, and (c) UV/Vis spectra of Al_2O_3-($PAR^1_{10\%}$ $PAR^2_{90\%}$) titrated with **SDBS** in DIW ($\lambda_{ext} = 408$ nm).

Scheme 5. Synthesis of the amphiphiles **DDPB**, **FC-PB**, **HC-PEG**, and **FC-PEG**.

nals of the perylene core at 392, 421, and 448 nm stayed unaffected. Because of an unchanged concentration of perylene during titration, the molecular density of the perylene core stayed constant (see Figure 1c). The same trend of intensifying fluorescence was observed for **Al_2O_3-($PAR^1_{10\%}$ $PAR^2_{90\%}$)** NPs, that were titrated with **SDS** or **DTAB** (Figure S5 and S8, Supporting Information). The UV/Vis spectra of those two systems stayed unaffected during the titration process, because of the optical inactive amphiphiles.

Further experiments on the optical properties of **Al_2O_3-($PAR^1_{10\%}$ $PAR^2_{90\%}$)** NPs focussing the perylene fluorescence, were done by using **DDPB** as a second-shell amphiphile (see Scheme 7). Figure 2a and b show that already after the first titration step with **DDPB**, resulting in a concentration of 0.10 mM, the fluorescence intensity of the perylene core drop. After the second titration step, the fluorescence intensity decreased more moderate and stayed constant at the same level during further titration with **DDPB** (see Figure 2b). The UV/Vis spectra in Figure 2c show an increase of the pyridinium absorption signal at 259 nm and constant perylene absorption bands during titration of **Al_2O_3-($PAR^1_{10\%}$ $PAR^2_{90\%}$)** with **DDPB**.

The differences in the optical properties of **[Al_2O_3-($PAR^1_{10\%}$ $PAR^2_{90\%}$)]SDBS** and **[Al_2O_3-($PAR^1_{10\%}$ $PAR^2_{90\%}$)]DDPB** NPs can also be seen from the visual appearance of the corresponding dispersions themselves. Figure 3a show the NP dispersions **[Al_2O_3-($PAR^1_{10\%}$ $PAR^2_{90\%}$)]SDBS** (right side) and **[Al_2O_3-($PAR^1_{10\%}$ $PAR^2_{90\%}$)]DDPB** (left side) under day-light conditions, both dis-

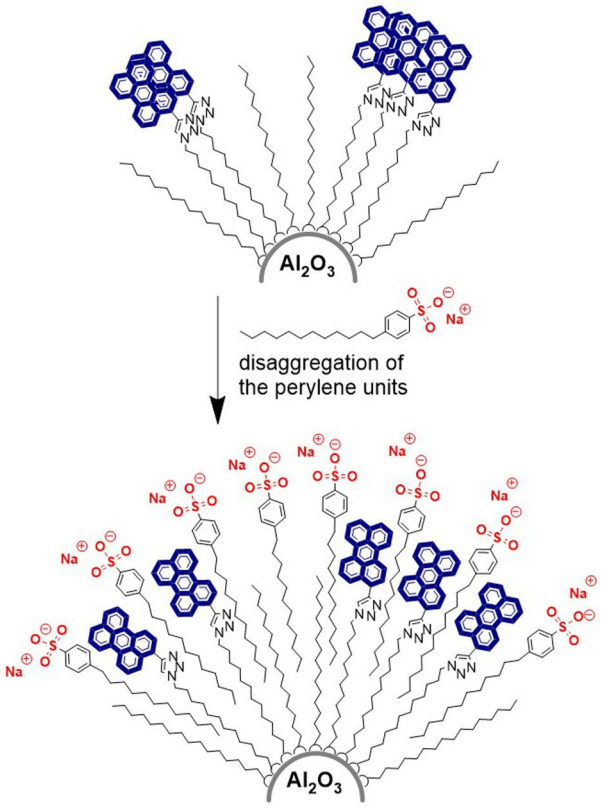

Scheme 6. Schematic representation of the formation of **[Al_2O_3-($PAR^1_{10\%}$ $PAR^2_{90\%}$)]SDBS** NPs.

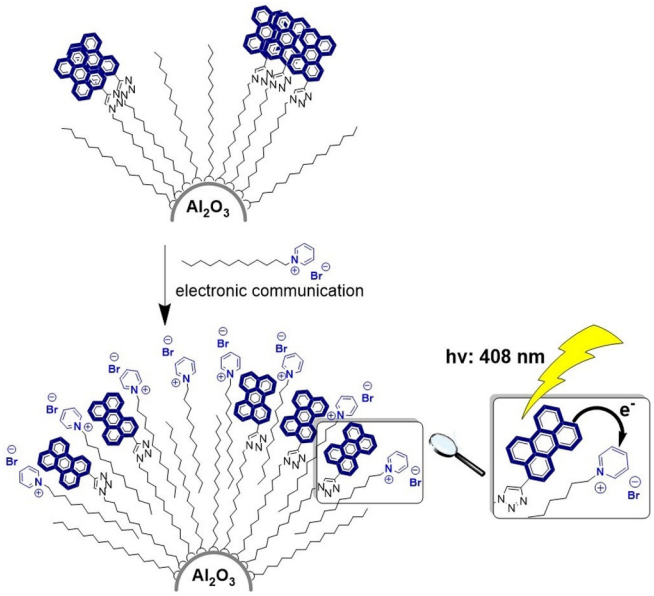

Scheme 7. Schematic representation of the formation of **[Al_2O_3-($PAR^1_{10\%}$ $PAR^2_{90\%}$)]DDPB** NPs with insights into the electronical behavior of the structure.

persions dispose of equivalent yellow colors. Under UV-light conditions (see Figure 3 b), the **[Al_2O_3-($PAR^1_{10\%}$ $PAR^2_{90\%}$)]SDBS** NPs show a strong yellowish-green fluorescence color, whereas

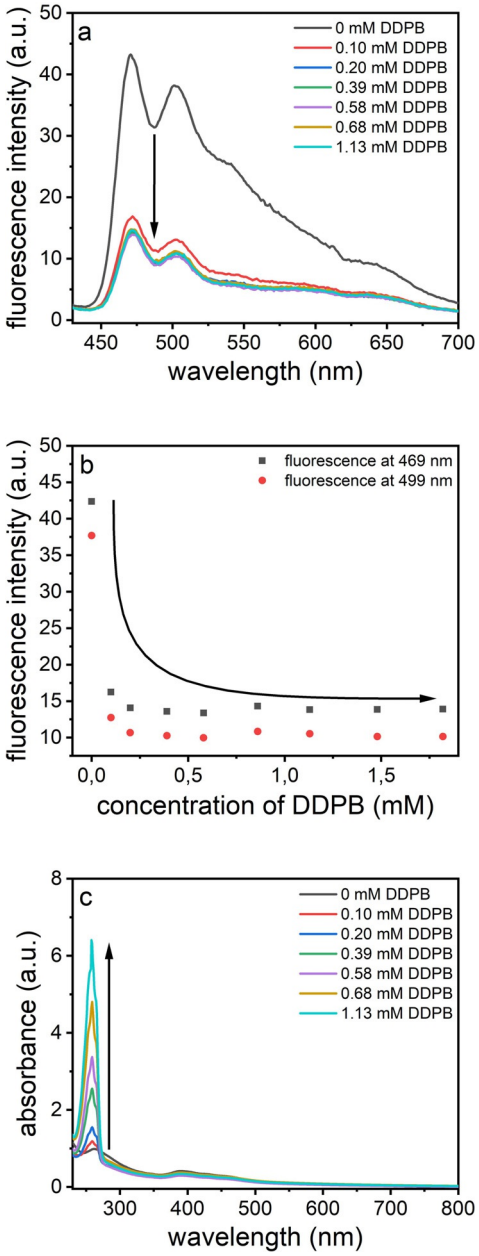

Figure 2. (a) Fluorescence spectra, (b) trend of the fluorescence spectra, and (c) UV/Vis spectra of **Al_2O_3-($PAR^1_{10\%}$ $PAR^2_{90\%}$)** titrated with **DDPB** in DIW ($\lambda_{ext} = 408$ nm).

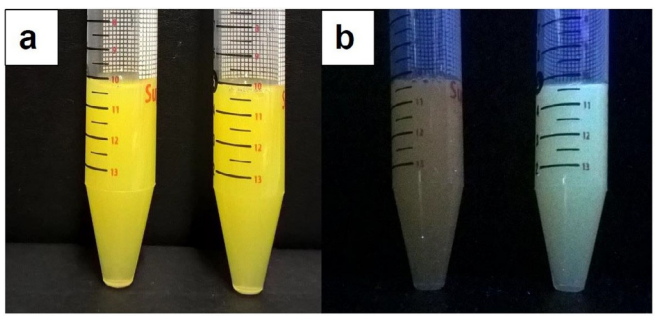

Figure 3. Optical appearance of **[Al_2O_3-($PAR^2_{10\%}$ $PAR^1_{90\%}$)]DDPB** (left side) and **[Al_2O_3-($PAR^2_{10\%}$ $PAR^1_{90\%}$)]SDBS** (right side) under (a) day-light and (b) UV-light conditions.

the **[Al_2O_3-($PAR^1_{10\%}$ $PAR^2_{90\%}$)]DDPB** NPs show a quenched fluorescence with a slightly orange fluorescence color.

In a next step, the nonionic amphiphile **HC-PEG**, was used to generate another family of *SbS*-functionalized NPs, namely **[Al_2O_3-($PAR^1_{10\%}$ $PAR^2_{90\%}$)]HC-PEG** (see Scheme 8). Figure 4a show the fluorescence measurements of **Al_2O_3-($PAR^1_{10\%}$ $PAR^2_{90\%}$)** NPs that were titrated with **HC-PEG** and in Figure 4b the trend of the fluorescence intensity of the **Al_2O_3-($PAR^1_{10\%}$ $PAR^2_{90\%}$)** NPs in dependence on the **HC-PEG** concentration is shown. After the first titration step, resulting in a concentration of 0.10 mM **HC-PEG**, the fluorescence band of the 0–0* transition (392 nm) strongly increased, also the fluorescence band of the 0–1* transition (421 nm) increased, but more moderately compared to the 0–0* transition. Additionally, the fluorescence signal of the 0–2* transition (448 nm) arise. Extra amount of **HC-PEG** had no further influence on the fluorescence properties of the NPs, the fluorescence signals of the perylene core stayed constant after the first titration step. In Figure 4c, the UV/Vis spectra of **[Al_2O_3-($PAR^1_{10\%}$ $PAR^2_{90\%}$)]HC-PEG** NPs during increasing amount of **HC-PEG**, were shown. From a concentration range from 0 mM to 0.20 mM **HC-PEG**, the initial UV/Vis spectrum stayed unaffected by increasing the amount of **HC-PEG** in the NP dispersion. During further titration with amphiphile, beginning at 0.29 mM **HC-PEG**, the overall absorption of the NPs increased and cloudy dispersions were formed.

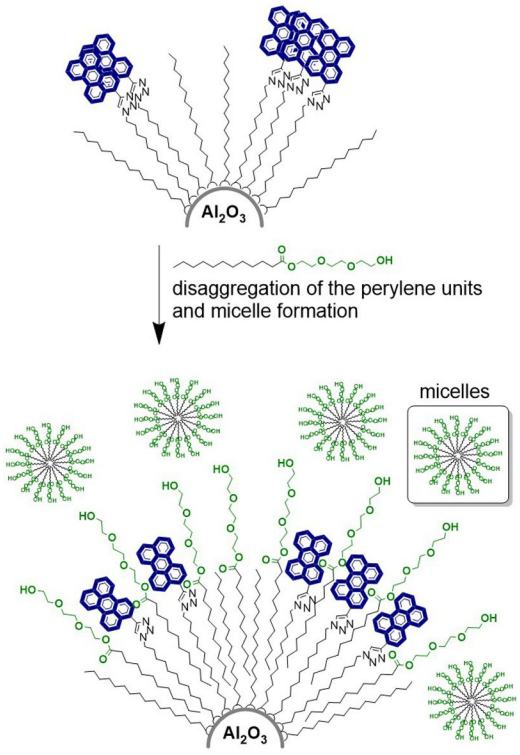

Scheme 8. Schematic representation of the formation of **[Al_2O_3-($PAR^1_{10\%}$ $PAR^2_{90\%}$)]HC-PG** NPs with excess of the **HC-PG** amphiphile forming NP-independent micelles.

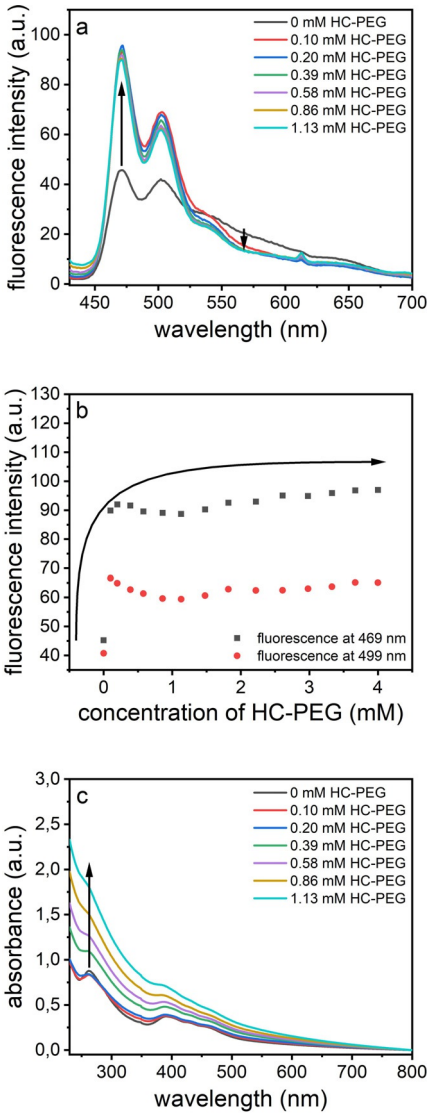

Figure 4. (a) Fluorescence spectra, (b) trend of the fluorescence spectra, and (c) UV/Vis spectra of **Al_2O_3-($PAR^1_{10\%}$ $PAR^2_{90\%}$)** titrated with **HC-PEG** in DIW (λ_{ext} = 408 nm).

Assembly of the fluorocarbon SbS-functionalized NPs

As an alternative to **Al_2O_3-($PAR^1_{10\%}$ $PAR^2_{90\%}$)** NPs, the fluorinated pendants were manufactured. The functionalization procedure was the same, but instead of using 90% **PAR^2**, 90% **PAR^3** was used as a spacing phosphonic acid, resulting in **Al_2O_3-($PAR^1_{10\%}$ $PAR^3_{90\%}$)** NP hybrids. The predominant coverage with **PAR^3** provides a fluorophilic surface (Scheme 2, Scheme 3).[4a,17] For the second functionalization step, amphiphiles with a fluorocarbon tail were used, for providing a successful assembly of the second layer around first-shell functionalized NPs. For this purpose we selected perfluoroundecanoic acid (**PFUnDA**), 1-(11-((3,3,4,4,5,5,6,6,7,7,8,8,9,9,10,10,10-heptadecafluorodecyl)oxy)-11-oxoundecyl)pyridin-1-ium bromide (**FC-PB**), or 2-(2-(2-hydroxyethoxy)ethoxy)ethyl 2,2,3,3,4,4,5,5,6,6,7,7,8,8,9,9,10,10,11,11,11-henicosafluoroundecanoate (**FC-PEG**).

In comparison to the hydrocarbon analogy **Al_2O_3-($PAR^1_{10\%}$ $PAR^2_{90\%}$)**, the **Al_2O_3-($PAR^1_{10\%}$ $PAR^3_{90\%}$)** NPs showed a better refined fluorescence spectrum with a more intense 0–0* transition (458 nm) compared to the 0–1* transition (484 nm). But the 0–2* transition band is also hidden. Figure 5a and b represent the fluorescence and UV/Vis measurements of **Al_2O_3-($PAR^1_{10\%}$ $PAR^3_{90\%}$)** NPs that were titrated with **PFUnDA** (Scheme 9). After the first titration step of **Al_2O_3-($PAR^1_{10\%}$ $PAR^3_{90\%}$)** with **PFUnDA**, resulting in a concentration of 0.10 mM, the perylene fluorescence was quenched and during further titration, the fluorescence band resulted in a broad undefined band that was shifted to higher wavelength. Starting from a concentration of 0.58 mM **PFUnDA**, the fluorescence spectrum did not further change. In the UV/Vis spectra of the **[Al_2O_3-($PAR^1_{10\%}$ $PAR^3_{90\%}$)]PFUnDA** NPs, shown in Figure 5b, it can be seen, that the optical density of the perylene core was unaffected during the titration experiment with **PFUnDA**.

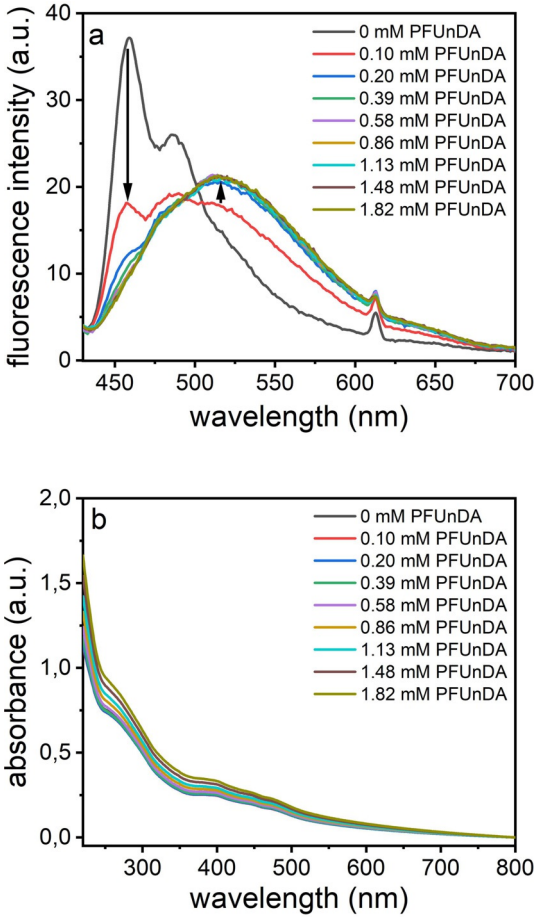

Figure 5. (a) Fluorescence spectra, (b) UV/Vis spectra of **Al_2O_3-($PAR^1_{10\%}$ $PAR^3_{90\%}$)** titrated with **PFUnDA** in DIW (λ_{ext} = 408 nm).

Next, **[Al_2O_3-($PAR^1_{10\%}$ $PAR^3_{90\%}$)]FC-PB** NPs were manufactured involving **FC-PB** as a special type of amphiphile within the second shell (see Scheme 10). **FC-PB** consists of a fluorocarbon moiety on one molecular end, the other end consists of a polar pyridinium bromide head-group generating the water-dispersibility. The fluorocarbon moiety and the polar head-group were bridged through a hydrocarbon spacer. That extraordinary type of amphiphile caused special fluorescence variations of **Al_2O_3-($PAR^1_{10\%}$ $PAR^3_{90\%}$)** NPs during the titration course with **FC-PB**. Figure 6a, b, and c show detailed fluores-

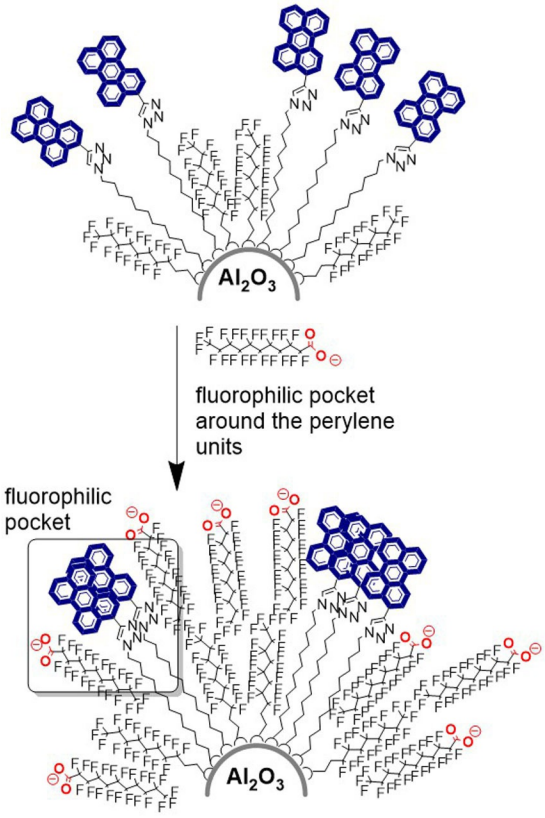

Scheme 9. Schematic representation of the formation of **[Al_2O_3-($PAR^1_{10\%}$ $PAR^3_{90\%}$)]PFUnDA** NPs, whereas **PFUnDA** formed a fluorophilic pocket around the perylene units.

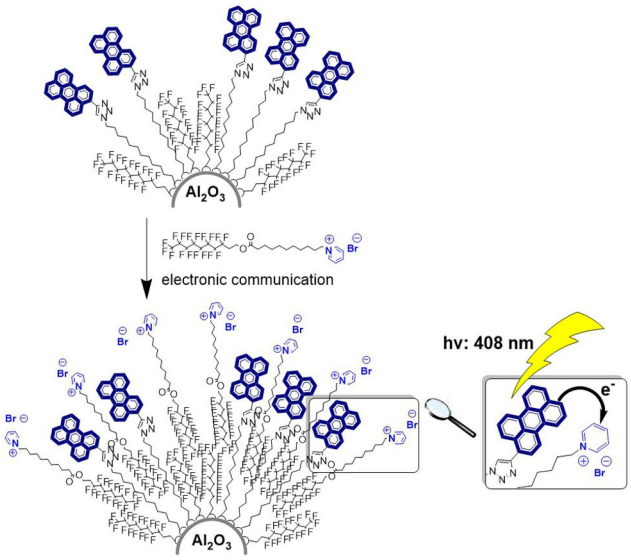

Scheme 10. Schematic representation of the formation of **[Al_2O_3-($PAR^1_{10\%}$ $PAR^3_{90\%}$)]FC-PB** NPs with insights into the electronical behavior of the system.

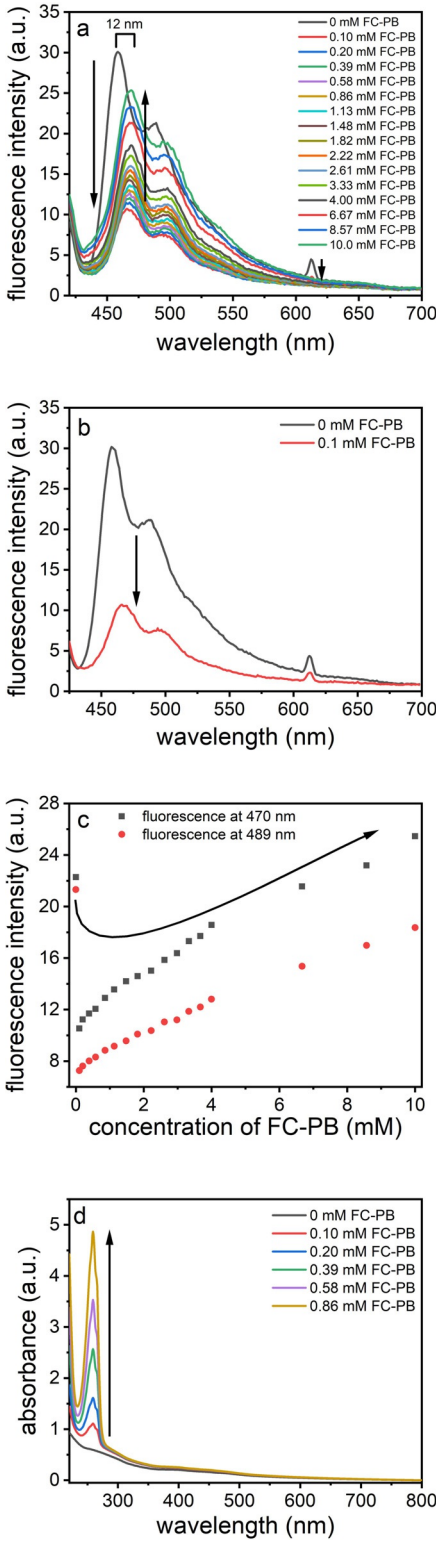

Figure 6. (a), (b) Fluorescence spectra, (c) trend of the fluorescence spectra, and (d) UV/Vis spectra of **Al_2O_3-($PAR^1_{10\%}$ $PAR^3_{90\%}$)** titrated with **FC-PB** in DIW (λ_{ext} = 408 nm).

cence measurements. The first titration step with the amphiphile applied in a concentration of 0.10 mM **FC-PB**, lead to a decreased perylene fluorescence. In the later course of the titration, the fluorescence of the perylene unit increased stepwise with increasing amount of **FC-PB**. Noticeable is also the fact, that the fluorescence band of the 0-0* transition of **[Al_2O_3-($PAR^1_{10\%}$ $PAR^3_{90\%}$)]FC-PB** is shifted around 12 nm to higher wavelength, compared to the system **Al_2O_3-($PAR^1_{10\%}$ $PAR^3_{90\%}$)** without amphiphile. Figure 6d represent the UV/Vis spectra of the NP system **Al_2O_3-($PAR^1_{10\%}$ $PAR^3_{90\%}$)** during titration with amphiphile **FC-PB**. The absorption signal of the pyridinium unit at 259 nm increased, whereas the optical density of the perylene core was constant during the titration experiment.

As a third example to study the optical properties of **Al_2O_3-($PAR^1_{10\%}$ $PAR^3_{90\%}$)** NPs during assembly of a second shell, the nonionic amphiphile **FC-PEG** was used (see Scheme 11). In Figure 7a and b the monitoring of the fluorescence and UV/Vis spectra of **[Al_2O_3-($PAR^1_{10\%}$ $PAR^3_{90\%}$)]FC-PEG** NPs in dependence on the amphiphile concentration is displayed. During titration with **FC-PEG**, the overall perylene fluorescence decreased. The fluorescence band of the 0–0* transition (458 nm) decreased stronger than that of the 0–1* transition (484 nm) and beginning with a concentration of 1.48 mM **FC-PEG**, there is just the leftover of a broad undefined fluorescence band. By looking at the UV/Vis spectra (see Figure 7b), no changes in the optical density of the perylene core were observed, because of a stable concentration of **Al_2O_3-($PAR^1_{10\%}$ $PAR^3_{90\%}$)** during titration with the optical inactive amphiphile **FC-PEG**.

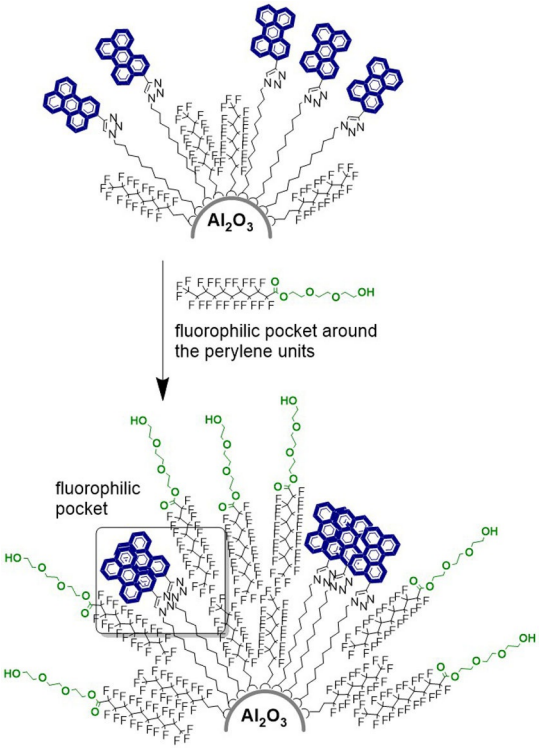

Scheme 11. Schematic representation of the formation of **[Al_2O_3-($PAR^1_{10\%}$ $PAR^3_{90\%}$)]FC-PEG** NPs, whereas **FC-PEG** formed a fluorophilic pocket around the perylene core.

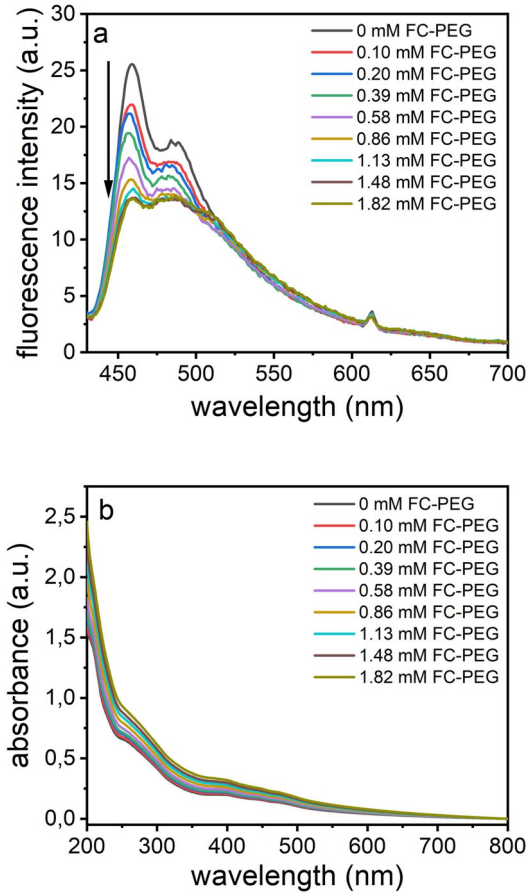

Figure 7. (a) Fluorescence spectra, and (b) UV/Vis spectra of **Al_2O_3-($PAR^1_{10\%}$ $PAR^3_{90\%}$)** titrated with **FC-PEG** in DIW (λ_{ext} = 408 nm).

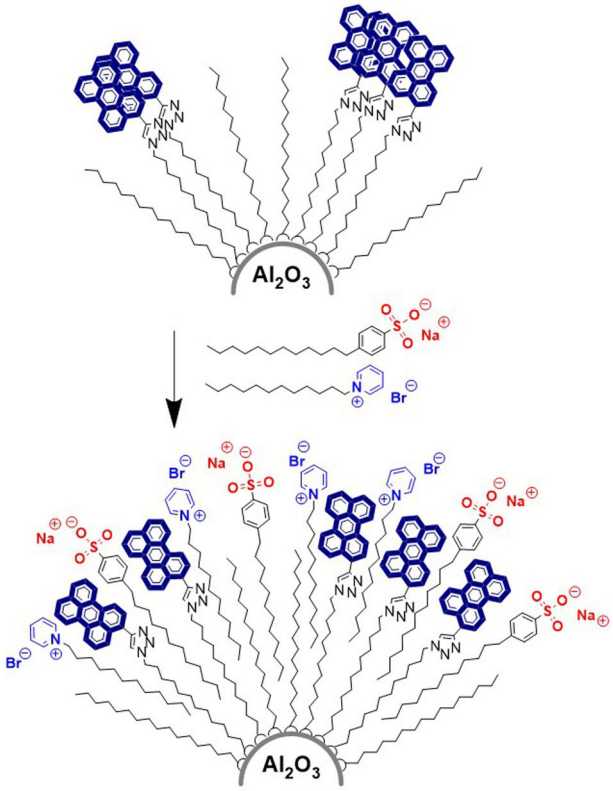

Scheme 12. Schematic representation of the formation of [**Al_2O_3-($PAR^1_{10\%}$ $PAR^2_{90\%}$)]SDBS&DDPB** NPs including a mixed second layer consisting of **SDBS** and **DDPB** in a one-to-one ratio.

Assembly of hydrocarbon SbS-functionalized NPs including a mixed second ligand shell

In a next step of complexity, a hydrocarbon *SbS*-architecture was generated including a mixed second ligand shell of **DDPB** and **SDBS**. That system is of high importance for comparative studies, because theoretically, it combines a fluorescence quencher and a fluorescence intensifier in one system. For this purpose, the first-shell functionalized hydrocarbon analogue **Al_2O_3-($PAR^1_{10\%}$ $PAR^2_{90\%}$)** was mixed with the second-shell ligands **DDPB** and **SDBS** in a ratio of 1:1 (Scheme 12), 1:2, or 2:1). It can be assumed, that the amphiphiles were attached roughly stoichiometrically onto the first-shell functionalized nanoparticles, as indicated by zeta-potential measurements of the mixed second-shell systems (see Supporting Information, Table S4). The fluorescence measurements showed in all three cases the same trend. There is one significant quenching step which could be matched to **DDPB** (Figure 8a, b) and in the further course of the titration, the fluorescence increased, initiated by **SDBS** (see Figure 8a and c, S6 and S7). Beginning at a total concentration of 1.13 mM **DDPB** and **SDBS** (1:1), the NPs formed flaky dispersions indicating that the electrosteric stabilization of the NPs could no longer be provided. Regarding the UV/Vis spectra, starting from a concentration of 0.86 mM **DDPB-SDBS** mixture, the absorption signal at 260 nm stayed constant.

Comparative analysis and theoretical interpretation of the obtained fluorescence studies during SbS-functionalization

First of all, the fact, that both starting materials, the lipophilic **Al_2O_3-($PAR^1_{10\%}$ $PAR^2_{90\%}$)** and the fluorophilic **Al_2O_3-($PAR^1_{10\%}$ $PAR^3_{90\%}$)** NPs vary in their fluorescence spectra, is striking. Whereas **Al_2O_3-($PAR^1_{10\%}$ $PAR^2_{90\%}$)** NPs give rise to undefined transition bands of the perylene core, **Al_2O_3-($PAR^1_{10\%}$ $PAR^3_{90\%}$)** NPs displayed more defined fluorescence signals. The undefined transition bands of **Al_2O_3-($PAR^1_{10\%}$ $PAR^2_{90\%}$)** NPs are characteristic for excimer formation of the perylene[12] units. Fluorocarbon moieties are more rigid than hydrocarbons[18] and are thus more suitable for separating the perylene cores onto the NP surface and prevent excimer formation, resulting in more structured fluorescence signals of the **Al_2O_3-($PAR^1_{10\%}$ $PAR^3_{90\%}$)** NPs. This has already been seen for pyrene and perylene bisimide functionalized Al_2O_3 NPs by using either hydrocarbon or fluorocarbon spacing phosphonic acids.[5,8]

The higher hierarchically assembled *SbS*-system **[Al_2O_3-($PAR^1_{10\%}$ $PAR^2_{90\%}$)]SDBS** displayed an increasing fluorescence intensity of **Al_2O_3-($PAR^1_{10\%}$ $PAR^2_{90\%}$)** during addition of **SDBS**, with refined 0–0*, 0–1* and 0–2* transition bands (Figure 1a and b). Very similar results were observed for the titrations of **Al_2O_3-($PAR^1_{10\%}$ $PAR^2_{90\%}$)** with **SDS** and **DTAB** (see Figure S5

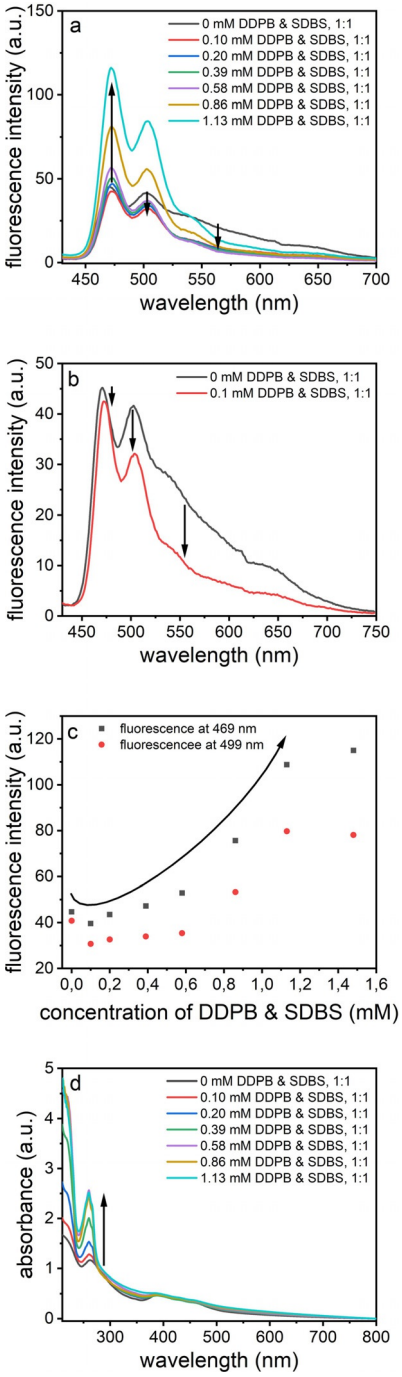

Figure 8. (a), (b) Fluorescence spectra, (c) trend of the fluorescence spectra, and (d) UV/Vis spectra of **Al_2O_3-($PAR^1_{10\%}$ $PAR^2_{90\%}$)** titrated with **DDPB** & **SDBS** (1:1) in DIW (λ_{ext} = 408 nm).

and S8, Supporting Information). During all three titration experiments, the form of the fluorescence spectra aligned to the reference fluorescence spectrum of the monomeric compound **3** in THF (Figure S4a). This is a proof, that the lipophilic moiety of **SDBS** (or **SDS**/**DTAB**) was incorporated into the first ligand shell, and lead to disaggregation of the perylene excimers[11] onto the NP surface.

By doing the same experiment with **DDPB** instead of **SDBS**, the fluorescence of the **Al_2O_3-($PAR^1_{10\%}$ $PAR^2_{90\%}$)** NPs was strongly quenched (Figure 2a and b). Reason for that phenomenon is an electronic communication between the pyridinium and the perylene unit. Pyridinium quenches the fluorescence of the perylene through a photo-induced electron-transfer (PET) from the excited state of the perylene, that was formed during excitation with light of 408 nm, towards the nitrogen atom of the pyridinium, that has a lowered LUMO energy level compared to that of the perylene.[6a,b,d,e,19]

By creating mixed second ligand shells, a combination of the amphiphiles **SDBS** and **DDPB** in a ratio of 1:1, 1:2, or 2:1, was titrated to **Al_2O_3-($PAR^1_{10\%}$ $PAR^2_{90\%}$)** NPs, while a new combination of effects has been arisen (Figure 8a and b, S6 and S7). After the first titration step, the fluorescence was quenched which could be matched to the **DDPB** that generated a PET from the perylene core to the pyridinium unit. By further titration, the effect of **SDBS** was predominant and the perylene fluorescence increased again, initiated by disaggregation of the perylene units onto the NP surface.

Manufacturing of **[Al_2O_3-($PAR^1_{10\%}$ $PAR^2_{90\%}$)]HC-PEG** NPs lead to an increased fluorescence intensity with well resolved fluorescence signals (Figure 3a and b), merely after the first titration step of **Al_2O_3-($PAR^1_{10\%}$ $PAR^2_{90\%}$)** with **HC-PEG**, resulting in a **HC-PEG** concentration of 0.10 mM. This fluorescence spectrum is already comparable to the monomeric fluorescence spectrum of reference compound **3** in THF (Figure S4a). Further addition of **HC-PEG** had no further influence on that fluorescence spectrum. These observations proof the successful formation of a lipophilic pocket among the perylene units and following separation of excimers. The single-step increase of the fluorescence and the formation of cloudy dispersions by further addition of **HC-PEG** indicate that pure micelles of the amphiphile were formed without interaction to the NP surface. This explanation could be strengthened by taking into account, that tetraethylene glycol monododecyl ether ($C_{12}EO_4$), an amphiphile with comparable molecular length and polarity to **HC-PEG**, has also a relatively low critical micelle concentration of around *cmc* = 0.046 mM.[20]

Coming to the fluorocarbon system, the first titration experiment was performed with **Al_2O_3-($PAR^1_{10\%}$ $PAR^3_{90\%}$)** and **PFUnDA**. During the formation of the *SbS*-system **[Al_2O_3-($PAR^1_{10\%}$ $PAR^3_{90\%}$)]PFUnDA**, it could be observed that the perylene fluorescence was quenched, already beginning at a concentration of 0.10 mM **PFUnDA** (see Figure 5a, b). Further addition of **PFUnDA** resulted in a broad undefined fluorescence band that was shifted to higher wavelengths, characteristic for excimers.[12a,21] At a concentration of 0.58 mM **PFUnDA**, the fluorescence spectrum stayed constant, at this point, the surface seems fully covered with amphiphile. Reason for the changes in the fluorescence spectra was a formation of a fluorophilic pocket around the perylene cores through incorporation of the fluorocarbon moiety of **PFUnDA** into the mainly fluorinated first-shell of the NPs (see Scheme 9). During this process, a phase separation of the hydrocarbons (**PAR^1**) from the fluorocarbons (**PAR^3**/**PFUnDA**)[22] onto the NP surface took place, which leads to a stronger interaction of the perylene units forming stacked complexes, so called excimers of the perylene,[12] resulting in a reduced fluorescence intensity with a

limited resolution of the characteristic fluorescence bands of the perylene.

During the formation of **[Al_2O_3-($PAR^1_{10\%}$ $PAR^3_{90\%}$)]FC-PB**, the fluorescence of **Al_2O_3-($PAR^1_{10\%}$ $PAR^3_{90\%}$)** was quenched after addition of 0.10 mM **FC-PB**, while the fluorescence band of the 0–0* transition of **[Al_2O_3-($PAR^1_{10\%}$ $PAR^3_{90\%}$)]FC-PB** is shifted around 12 nm to higher wavelength, compared to the system **Al_2O_3-($PAR^1_{10\%}$ $PAR^3_{90\%}$)** without amphiphile. The quenching effect as well as the shift of the fluorescence band are signals for an electronical communication between the perylene core and the pyridinium unit. The forthgoing titration displayed a stepwise increase of the fluorescence with increasing amount of **FC-PB**. It is thus comparable to the hydrocarbon *SbS*-functionalized system including a mixed second ligand shell of SDBS and DDPB. When the fluorocarbon moiety of **FC-PB** was incorporated into the fluorinated first-shell of the **Al_2O_3-($PAR^1_{10\%}$ $PAR^3_{90\%}$)** NPs, the hydrocarbon spacing unit of the amphiphile **FC-PB** was positioned around the perylene core and separated the perylene units onto the NP surface which goes hand-in-hand with an increased fluorescence intensity of the perylene signals. The absent formation of a broad undefined excimer band signals that in this case no fluorophilic pocket was formed among the perylene core.

During the *SbS*-formation of **[Al_2O_3-($PAR^1_{10\%}$ $PAR^3_{90\%}$)]FC-PEG**, the fluorescence signals changed into a broad undefined excimeric fluorescence band. These results are very similar to those of **[Al_2O_3-($PAR^1_{10\%}$ $PAR^3_{90\%}$)]PFUnDA**. This is also a successful proof for the formation of fluorophilic pockets around the perylene units causing stack formation.

Biological experiments

Fluorescent dyes and proteins are used in immunofluorescent assay, live cell or in vivo animal imaging. Long observation times and cell autofluorescence in the visible spectrum leads to the search for new fluorescent markers with high quantum yields, large saturation intensities and good biocompatibility. Because of their excellent fluorescence properties, the NPs **[Al_2O_3-($PAR^1_{10\%}$ $PAR^2_{90\%}$)]SDBS**, and **[Al_2O_3-($PAR^1_{10\%}$ $PAR^2_{90\%}$)]DTAB**, functionalized with **PAR^1** and **PAR^2** in the first shell and amphiphiles fused of hydrocarbons and polar headgroups with contrary surface charge, were tested for their application in fluorescence imaging in different cell lines (A549-lung cancer cells, HUVEC-endothelial cells, MCF-10 A-breast epithelial cells, and MDA-MB-231-breast cancer cells). These NPs are excellent dispersible in water. Both kinds of *SbS*-functionalized nanoparticles exhibit a hydrodynamic diameter of 100 nm (Table 1, Figure S12 and S15) in water. Compared to the diameter size of 14 nm obtained by BET and TEM measurements (Figure S1 and S2), the size is quite enlarged. The hydrodynamic diameter obtained by DLS measurements of the pristine NPs are below 50 nm (Figure S11). This indicating already some clustering of the pristine NPs. Therefore, it is possible that polynuclear clusters form the center of the *SbS*-functionalized NPs. However, biological fluids have a different ionic strength compared to the ultrapure water and is additionally enriched with proteins and other biological substances that can form the so-called protein corona on the surface of the NPs. Supplementary to the DLS measurements of a 0.015 wt% NP dispersion in water, the same measurements were conducted with NPs in cell culture medium enriched with 10% fetal calf serum (FCS) as a protein source. The hydrodynamic diameter of the **[Al_2O_3-($PAR^1_{10\%}$ $PAR^2_{90\%}$)]SDBS** decreases in cell culture medium, whereas the diameter of the **[(Al_2O_3-($PAR^1_{10\%}$ $PAR^2_{90\%}$)]DTAB** NPs increases (Table 1). With hydrodynamic size of around 46 nm in cell medium, the attached biomolecules provide an even better dispersibility of **[Al_2O_3-($PAR^1_{10\%}$ $PAR^2_{90\%}$)]SDBS** NPs in medium than in water. The **[Al_2O_3-($PAR^1_{10\%}$ $PAR^2_{90\%}$)]SDBS** NPs with the protein shell become single particles or very small aggregates (Figure S20). After incubation of the NPs in serum enriched buffer solution, proteins or other biomolecules of the solution became attached to the surface. To determine the change in the surface potential, the NPs were collected by centrifugation and re-dispersed in water. The zeta potential is reduced but still negative. The hydrodynamic diameter of **[(Al_2O_3-($PAR^1_{10\%}$ $PAR^2_{90\%}$)]DTAB** NPs is around 149 nm with a broad size distribution in the DLS measurements (Figure S21). Since the diameter of the NPs are much smaller and it is very unlikely, that the attachment of the coating and protein corona expands a single particle to this size, these NPs form larger agglomerates than the **[(Al_2O_3-($PAR^1_{10\%}$ $PAR^2_{90\%}$)]DTAB** NPs. The zeta potential turns from positive to negative charge, which indicates that the surface charge is determined by the charge of proteins and biomolecules attached. Since the zeta potential of both particles after protein attachment is similar, only the surface attached proteins of the serum define now the zeta potential of the NPs. In a next step the amount of protein at the NPs surface was measured. Both NPs were incubated in a PBS solution with 1% FCS overnight and afterwards the amount of proteins on the surface was determined. The proteins are getting adsorbed on the surface of single particles, smaller or larger aggregates forming a small shell around these. Since both NP solutions contain the same concentration, the larger agglomerates of the **[Al_2O_3-($PAR^1_{10\%}$ $PAR^2_{90\%}$)]DTAB** NPs form fewer particles than the smaller sized aggregates of the **[Al_2O_3-($PAR^1_{10\%}$ $PAR^2_{90\%}$)]SDBS** NPs and therefore a lesser amount of proteins is needed to surround these NPs as can be seen in Table 1.

Table 1. DLS (intensity in number) and zeta-potential measurements of the **[Al_2O_3-($PAR^1_{10\%}$ $PAR^2_{90\%}$)]SDBS** and **[Al_2O_3-($PAR^1_{10\%}$ $PAR^2_{90\%}$)]DTAB** NPs in water and cell culture medium with 10% serum and amount of proteins attached onto the particle surface.

	DLS (water)	ζ (water)	DLS (medium)	ζ (water)	Mass of protein/1 mg NP
[Al_2O_3-($PAR^1_{10\%}$ $PAR^2_{90\%}$)]SDBS	100.89 ± 6.80 nm	−58.0 ± 2.46 mV	46.13 ± 4.00 nm	−26.4 ± 1.89 mV	0.80 mg protein/mg NP
[Al_2O_3-($PAR^1_{10\%}$ $PAR^2_{90\%}$)]DTAB	100.89 ± 6.80 nm	+33.8 ± 2.87 mV	149.27 ± 12.93 nm	−32.8 ± 0.651 mV	0.38 mg protein/mg NP

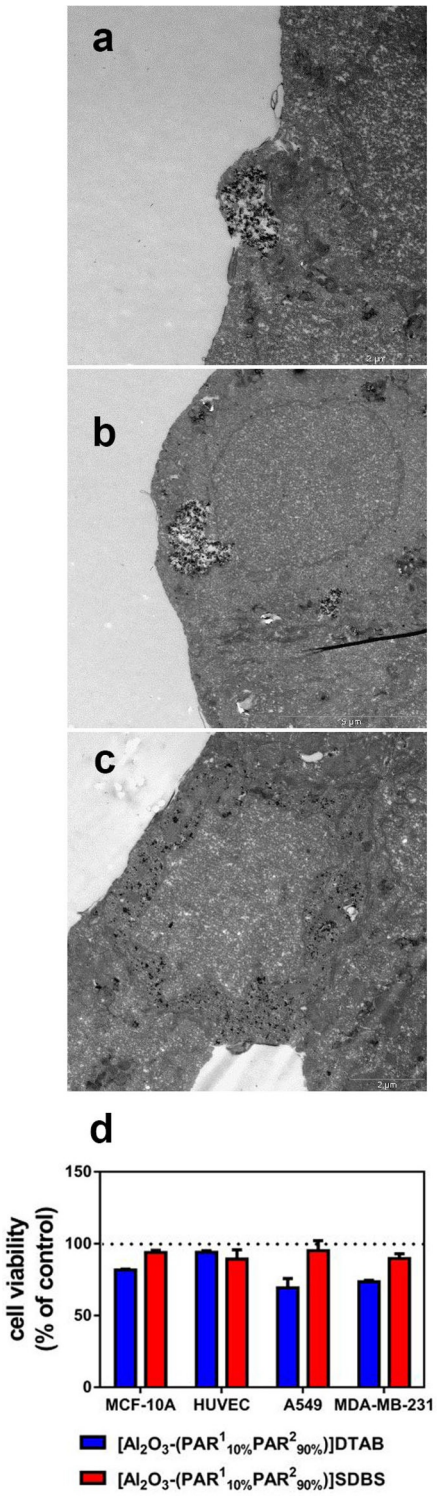

Figure 9. TEM images of the A549 cells with (a, b) **[Al_2O_3-($PAR^1_{10\%}$ $PAR^2_{90\%}$)]DTAB**, (c) **[Al_2O_3-($PAR^1_{10\%}$ $PAR^2_{90\%}$)]SDBS** and (d) biocompatibility of the NPs to the different used cell lines.

The size of the NP aggregates also determines the way NPs were taken up by cells and their localization inside the cells[23] (Figure 9a–c). The large agglomerates of the NPs enter the cells via endocytosis most likely macro-pinocytosis. Macro-pinocytosis involves the formation of actin filament driven plasma membrane protrusion, which finally covers the large agglomerates of the NPs (see Figure 9a). Finally a large vesicle, the micropinosome, loaded with these NPs is formed (see Figure 9b).[24] The well dispersed **[Al_2O_3-($PAR^1_{10\%}$ $PAR^2_{90\%}$)]SDBS** can be found in small NP clusters or single particles distributed in the whole cytoplasm (Figure 9c). These particles are not found inside of vesicles like the **[Al_2O_3-($PAR^1_{10\%}$ $PAR^2_{90\%}$)]DTAB**. The absence of vesicles, which are built during endocytosis, indicates a different uptake mechanism like a direct diffusion through the plasma membrane.[7] Both NPs were tested for their biocompatibility via the neutral red assay in all different cell lines. The **[Al_2O_3-($PAR^1_{10\%}$ $PAR^2_{90\%}$)]SDBS** NPs show nearly no cytotoxic effects on the non-cancerous as well as the cancerous cell lines, when cultivated for 24 h in cell culture medium containing 50 $\mu g\,mL^{-1}$ NPs (Figure 9d). In contrast, the **[Al_2O_3-($PAR^1_{10\%}$ $PAR^2_{90\%}$)]DTAB** NPs are more toxic for the A549, MDA-MB-231 and MCF-10 A cells than the **[Al_2O_3-($PAR^1_{10\%}$ $PAR^2_{90\%}$)]SDBS** NPs.

The different uptake mechanisms are also reflected in the fluorescent images of the cells. To ensure, that the attached protein shell and the retention time of the NPs in cell culture medium, does not change the absorption and fluorescence of the NPs, long term stability UV/Vis and fluorescence measurements were conducted (Figure S10). After 58 h no change in the UV/Vis absorption or fluorescence can be detected. The fluorescent **[Al_2O_3-($PAR^1_{10\%}$ $PAR^2_{90\%}$)]DTAB** NPs build large green spots, which surround the blue stained cell nucleus of the A549 cells (Figure 10a) and HUVECs (Figure 10c). The large green spots represent the agglomerates of NPs concentrated inside the vesicles. The **[Al_2O_3-($PAR^1_{10\%}$ $PAR^2_{90\%}$)]SDBS** NPs appear as small green dots or a blurry shell around the cell nucleus of the A549 cells (Figure 10b). These NPs are evenly distributed throughout the whole cytoplasm. The concentration of the **[Al_2O_3-($PAR^1_{10\%}$ $PAR^2_{90\%}$)]DTAB** NPs inside of the macropinosomes lead to a higher fluorescent signal inside the cells than the evenly distributed **[Al_2O_3-($PAR^1_{10\%}$ $PAR^2_{90\%}$)]SDBS**

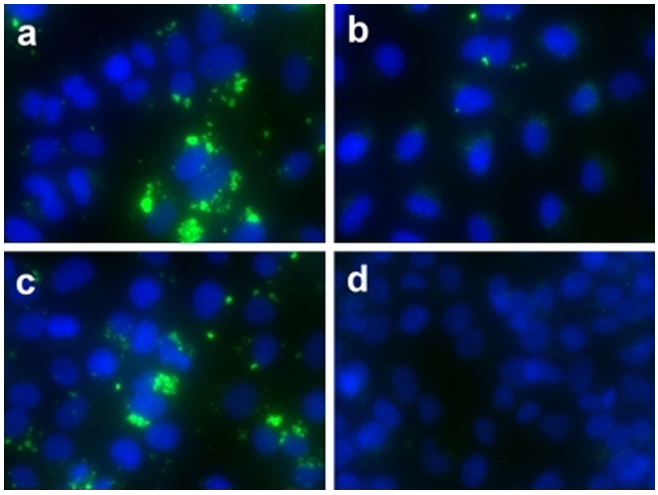

Figure 10. Fluorescent images of the A549 cells with (a) [Al_2O_3-($PAR^1_{10\%}$ $PAR^2_{90\%}$)]DTAB, (b) [Al_2O_3-($PAR^1_{10\%}$ $PAR^2_{90\%}$)]SDBS and HUVEC cells with (c) [Al_2O_3-($PAR^1_{10\%}$ $PAR^2_{90\%}$)]DTAB and (d) the [Al_2O_3-($PAR^1_{10\%}$ $PAR^2_{90\%}$)]SDBS NPs.

NPs. No green fluorescent can be seen inside the cytoplasm of the HUVECs (Figure 10 d). A similar behavior can are recognized for the MDA-MB-231 and MCF-10 A cells (Figure S22).

To test if the fluorescent signal of **[Al_2O_3-($PAR^1_{10\%}$ $PAR^2_{90\%}$)]SDBS** is to low inside the cells or the concentration of these NPs is really much smaller inside the HUVECs, the concentration of the NPs inside the cells was detected. The fluorescent intensity was correlated with the concentration of the different NPs and normalized to the cell number. For the fluorescent images the concentration of **[Al_2O_3-($PAR^1_{10\%}$ $PAR^2_{90\%}$)]DTAB** NPs is clearly greater inside all cell lines than that of the **[Al_2O_3-($PAR^1_{10\%}$ $PAR^2_{90\%}$)]SDBS** NPs (Figure 11 a),

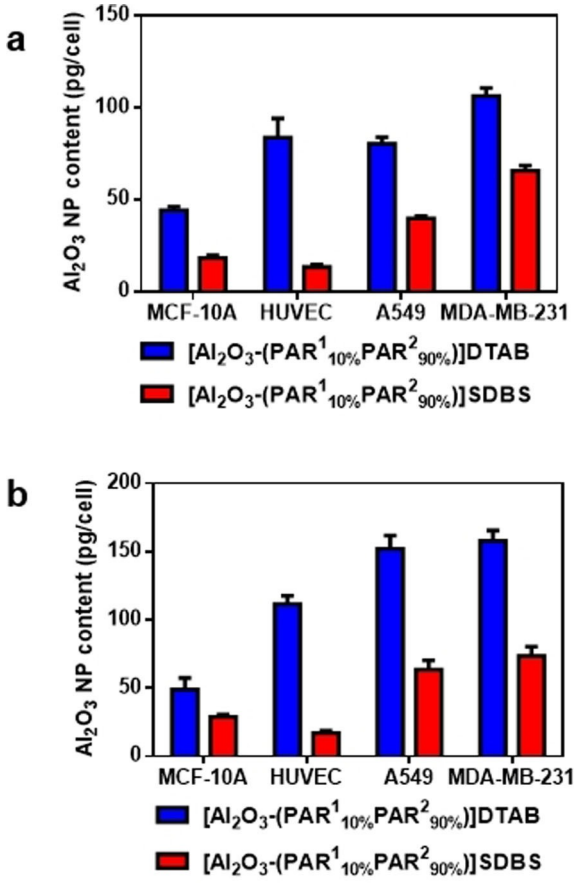

Figure 11. Determination of the intracellular NP content either by (a) fluorescent intensity or by (b) ICP-AAS measurements.

but compared to the non-cancerous HUVECs and MCF-10 A cells the amount of **[Al_2O_3-($PAR^1_{10\%}$ $PAR^2_{90\%}$)]SDBS** is still much higher inside the cancerous A549 and MDA-MB-231 cells. To test if these results reflect the actual concentration of the NPs inside the cells, the amount of aluminum was determined via ICP-AAS and also normalized to the cell number. For a better comparability the aluminum concentration of the NPs was measured and so the NP concentration per cell was stated (Figure 11 b). The determination of the mass of NPs via ICP-AAS shows very similar results to the measurements via the fluorescent imaging. The smaller aggregates or single NPs of the **[Al_2O_3-($PAR^1_{10\%}$ $PAR^2_{90\%}$)]SDBS** dispersion are hardly penetrate the cellular membranes of the non-cancerous cells, in contrast to the cancerous cells. The structure and composition of the plasma membrane as well as its biophysical status regulates the intracellular uptake of different substances. The rapid proliferation of cancer cells leads to a frequently need of membrane lipids and proteins. Therefore, their biosynthetic pathways are modified and up-regulated in cancer cells, which is followed by a continuous production of alterations in lipids or proteins. The nature of these changes determines the properties and uptake mechanics of the cancer cell membrane, which differs from the uptake behavior of healthy cells like HUVEC and MCF-10 A.[25]

Conclusions

We reported on a series of *SbS*-functionalized Al_2O_3 NPs involving a perylene terminated phosphonic acid as a fluorescence marker in the first ligand shell in combination with a hydrocarbon or a fluorocarbon terminated phosphonic acid as well as amphiphiles in the second ligand shell. Already the combination of the perylene phosphonic acid with the matrix phosphonic acids leads to different fluorescence features of the perylene core. For the second-shell functionalization, amphiphiles consisting of a hydrocarbon or fluorocarbon moiety were used. The interdigitation of the amphiphiles into the first ligand shell leads to unique changes in the fluorescence properties of the NP hybrids. The changes in the fluorescence are associated to disaggregation or aggregation of the perylene units through formation of a lipophilic or fluorophilic pocked among the perylene units. An increase in fluorescence and creation of more refined fluorescence signals was observed for disaggregation of the perylene units, whereas a decrease of fluorescence sets in when the perylene units are forced to aggregate. Furthermore, the perylene fluorescence of first-shell functionalized NPs was reduced by implementation of amphiphiles involving a pyridinium head-group, due to the establishment of a photo-induced electron-transfer from the perylene towards the pyridinium building block. After studying a series of examples of water-dispersible NPs, we selected two systems with excellent fluorescence features and opposite surface charges, namely **[Al_2O_3-($PAR^1_{10\%}$ $PAR^2_{90\%}$)]SDBS** and **[Al_2O_3-($PAR^1_{10\%}$ $PAR^2_{90\%}$)]DTAB**, for biological applications. These NPs differ in their dispersibility in the cell culture medium. The **[Al_2O_3-($PAR^1_{10\%}$ $PAR^2_{90\%}$)]DTAB** NPs form large agglomerates surrounded by a protein corona that change their surface charge. These large particles were taken up by all used cells to a large extend via macro-pinocytosis. The **[Al_2O_3-($PAR^1_{10\%}$ $PAR^2_{90\%}$)]SDBS** NPs are well dispersible forming individualized NPs or very small aggregates surrounded by a still negatively charged protein shell. These NPs cross the membranes of the cancer cells by penetration and are afterwards evenly distributed in the cytoplasm. In fluorescent imaging the large agglomerates of the **[Al_2O_3-($PAR^1_{10\%}$ $PAR^2_{90\%}$)]DTAB** NPs inside vesicles can be easier spotted than the single, widespread **[Al_2O_3-($PAR^1_{10\%}$ $PAR^2_{90\%}$)]SDBS** NPs. In upcoming studies of our laboratory these excellent fluorescent probes will be developed for

their use in multicellular tumor spheroids. With the help of the fluorescent signal, the pathway and penetration depth of NPs inside this several micrometers large tumor spheroids will be followed.

Acknowledgements

We thank the Cluster of Excellence "Engineering of Advanced Materials" (EAM) andthe SFB 953 "Synthetic Carbon Allotropes" funded by the German Research Council (DFG) as well as the Graduate School Advanced Materials and Processes (GS AMP) for financial support. We also thank the Chair of Chemical Reaction Engineering (CRT) in Erlangen for the BET measurement, Tobias Weißenberger (Institute of Chemical Reaction Engineering, University Erlangen-Nuremberg) for the ICP-AAS measurements, and Tobias Luchs for the Cover Design. Open access funding enabled and organized by Projekt DEAL.

Conflict of interest

The authors declare no conflict of interest.

Keywords: amphiphiles · fluorescent imaging · hydro-, lipo-, fluoro-philic/phobic · perylene chromophore · shell-by-shell (SbS)-functionalization

[1] a) L. Zeininger, S. Petzi, J. Schönamsgruber, L. Portilla, M. Halik, A. Hirsch, *Chem. Eur. J.* **2015**, *21*, 14030 – 14035; b) L. M. S. Stiegler, T. Luchs, A. Hirsch, *Chem. Eur. J.* **2020**, *26*, 8483 – 8498.
[2] a) S. P. Pujari, L. Scheres, A. T. Marcelis, H. Zuilhof, *Angew. Chem. Int. Ed.* **2014**, *53*, 6322 – 6356; *Angew. Chem.* **2014**, *126*, 6438 – 6474; b) H. Dietrich, T. Schmaltz, M. Halik, D. Zahn, *Phys. Chem. Chem. Phys.* **2017**, *19*, 5137 – 5144.
[3] T. Pellegrino, L. Manna, S. Kudera, T. Liedl, D. Koktysh, A. L. Rogach, S. Keller, J. Raedler, G. Natile, W. J. Parak, *Nano. Lett.* **2004**, *4*, 703 – 707.
[4] a) L. Zeininger, L. M. S. Stiegler, L. Portilla, M. Halik, A. Hirsch, *ChemistryOpen* **2018**, *7*, 282 – 287; b) L. Portilla, M. Halik, *ACS Appl. Mater. Interfaces* **2014**, *6*, 5977 – 5982; c) S. A. Paniagua, P. J. Hotchkiss, S. C. Jones, S. R. Marder, A. Mudalige, F. S. Marrikar, J. E. Pemberton, N. R. Armstrong, *J. Phys. Chem. C* **2008**, *112*, 7809 – 7817.
[5] J. E. Wittmann, L. M. S. Stiegler, C. Henkel, J. Träg, K. Götz, T. Unruh, D. Zahn, A. Hirsch, D. Guldi, M. Halik, *Adv. Mater. Interfaces* **2019**, *6*, 1801930.
[6] a) D. A. Wade, C. Mao, A. C. Hollenbeck, S. A. Tucker, *Frenzius J. Anal. Chem.* **2001**, *369*, 378 – 384; b) D. A. Wade, S. A. Tucker, *Talanta* **2000**, *53*, 571 – 578; c) S. Pandey, L. E. Roy, J. C. Fetzer, W. E. Acree, *Talanta* **1999**, *48*, 1103 – 1110; d) S. Pandey, W. E. Acree, J. C. Fetzer, *Talanta* **1998**, *47*, 769 – 778; e) S. Pandey, W. E. Acree, J. C. Fetzer, *Talanta* **1997**, *45*, 39 – 45.
[7] U. Breymann, H. Dreeskamp, E. Koch, M. Zander, *Chem. Phys. Lett.* **1978**, *59*, 68 – 70.
[8] C. Henkel, J. E. Wittmann, J. Trag, J. Will, L. M. S. Stiegler, P. Strohriegl, A. Hirsch, T. Unruh, D. Zahn, M. Halik, D. M. Guldi, *Small* **2020**, *16*, 1903729.
[9] L. M. S. Stiegler, A. Hirsch, *Chem. Eur. J.* **2019**, *25*, 11864 – 11875.
[10] S. Klein, L. M. S. Stiegler, C. Harreiss, L. V. R. Distel, W. Neuhuber, E. Spiecker, A. Hirsch, C. Kryschi, *ACS Appl. Biol. Mater.* **2018**, *1*, 2002 – 2011.
[11] D. Zhai, W. Xu, L. Zhang, Y. T. Chang, *Chem. Soc. Rev.* **2014**, *43*, 2402 – 2411.
[12] a) J. B. Birks, *Rep. Prog. Phys.* **1975**, *38*, 903 – 974; b) R. Katoh, S. Sinha, S. Murata, M. Tachiy, *J. Photoch. Photobio. A* **2001**, *145*, 23 – 34.
[13] S. H. Etschel, L. Portilla, J. Kirschner, M. Drost, F. Tu, H. Marbach, R. R. Tykwinski, M. Halik, *Angew. Chem. Int. Ed.* **2015**, *54*, 9235 – 9238; *Angew. Chem.* **2015**, *127*, 9367 – 9370.
[14] a) D. Jordan, E. Tan, D. Hegh, *J. Surfactants Deterg.* **2012**, *15*, 587 – 592; b) T. Luchs, M. Sarcletti, L. Zeininger, L. Portilla, C. Fischer, S. Harder, M. Halik, A. Hirsch, *Chem. Eur. J.* **2018**, *24*, 13589 – 13595.
[15] L. Zeininger, L. Portilla, M. Halik, A. Hirsch, *Chem. Eur. J.* **2016**, *22*, 13506 – 13512.
[16] C. M. Jäger, T. Schmaltz, M. Novak, A. Khassanov, A. Vorobiev, M. Hennemann, A. Krause, H. Dietrich, D. Zahn, A. Hirsch, M. Halik, T. Clark, *J. Am. Chem. Soc.* **2013**, *135*, 4893 – 4900.
[17] P. J. Hotchkiss, S. C. Jones, S. A. Paniagua, A. Sharma, B. Kippelen, N. R. Armstrong, S. R. Marder, *Acc. Chem. Res.* **2012**, *45*, 337 – 346.
[18] a) L. M. Wilson, A. C. Griffin, *Macromolecules* **1993**, *26*, 6312 – 6314; b) L. M. Wilson, A. C. Griffin, *Macromolecules* **1994**, *27*, 1928 – 1931; c) J. Träg, D. Zahn, *J. Mol. Model.* **2019**, *25*, 39.
[19] S. Pandey, W. E. Acree, J. C. Fetzer, *Mikrochim. Acta* **1998**, *129*, 41 – 45.
[20] a) E. Rodenas, M. Valiente, M. d. S. Villafruela, *J. Phys. Chem. B* **1999**, *103*, 4549 – 4554; b) J. J. Haftka, P. Scherpenisse, G. Oetter, G. Hodges, C. V. Eadsforth, M. Kotthoff, J. L. Hermens, *Environ. Toxicol. Chem.* **2016**, *35*, 2173 – 2181; c) S. Yuan, Z. Cai, G. Xu, Y. Jiang, *Colloid. Polym. Sci.* **2002**, *280*, 630 – 636.
[21] a) J. B. Birks, L. G. Christophorou, *Nature* **1963**, *197*, 1064 – 1065; b) J. B. Birks, *J. Phys. Chem.* **1963**, *67*, 2199 – 2200; c) J. B. Birks, L. G. Christophorou, *Spechtrochim. Acta* **1963**, *19*, 401 – 410; d) J. B. Birks, L. G. Christophorou, *Nature* **1962**, *194*, 442 – 444.
[22] a) P. Mukerjee, A. Y. S. Yang, *J. Phys. Chem.* **1976**, *80*, 1388 – 1390; b) P. Lo Nostro, *Adv. Colloid Interface Sci.* **1995**, *56*, 245 – 287; c) K. Shinoda, T. Nomura, *J. Phys. Chem.* **1980**, *84*, 365 – 369; d) T. Kunitake, S.-i. Tawaki, N. Nakashima, *Bull. Chem. Soc. Jpn.* **1983**, *56*, 3235 – 3242.
[23] a) L. Treuel, X. Jiang, G. U. Nienhaus, *J. R. Soc. Interface* **2013**, *10*, 20120939; b) S. Ritz, S. Schöttler, N. Kotman, G. Baier, A. Musyanovych, J. Kuharev, K. Landfester, H. Schild, O. Jahn, S. Tenzer, V. Mailänder, *Biomacromolecules* **2015**, *16*, 1311 – 1321; c) J. Llop, I. Estrela-Lopis, R. F. Ziolo, A. González, J. Fleddermann, M. Dorn, V. G. Vallejo, R. Simon-Vazquez, E. Donath, Z. Mao, C. Gao, S. E. Moya, *Part. Part. Syst. Charact.* **2014**, *31*, 24 – 35; d) N. Ma, C. Ma, C. Li, T. Wang, Y. Tang, H. Wang, X. Mou, Z. Chen, N. He, *J. Nanosci. Nanotechnol.* **2013**, *13*, 6485 – 6498.
[24] S. T. Stern, P. P. Adiseshaiah, R. M. Crist, *Part. Fibre Toxicol.* **2012**, *9*, 20 – 35.
[25] a) N. Bernardes, A. M. Fialho, *Int. J. Mol. Sci.* **2018**, *19*, 3871 – 3890; b) T. Galeotti, S. Borello, G. Minotti, L. Masotti, *N. Y. Acad. Sci.* **1986**, *488*, 468 – 480.

Manuscript received: July 8, 2020
Revised manuscript received: August 5, 2020
Accepted manuscript online: August 17, 2020
Version of record online: November 30, 2020